Performance Evaluation of Electronic Inductor-Based Adjustable Speed Drives with Respect to Line Current Interharmonics

Soltani, Hamid; Davari, Pooya; Blaabjerg, Frede; Zare, Firuz

Published in:
Proceedings of the 2017 IEEE Applied Power Electronics Conference and Exposition (APEC)

DOI (link to publication from Publisher):
10.1109/APEC.2017.7931150

Publication date:
2017

Document Version
Accepted author manuscript, peer reviewed version

Performance Evaluation of Electronic Inductor Based Adjustable Speed Drives with Respect to Line Current Interharmonics

Hamid Soltani, Pooya Davari, and Frede Blaabjerg
Department of Energy Technology
Aalborg University
Aalborg East, Denmark
hso@et.aau.dk, pda@et.aau.dk, fbl@et.aau.dk

Firuz Zare
Power and Energy Systems
University of Queensland
Brisbane St Lucia Qld 4072, Australia
f.zare@uq.edu.au

***Abstract*—Electronic Inductor (EI)-based front-end rectifiers have a large potential to become the next generation of Active Front End (AFE) topology used in many applications including Adjustable Speed Drives (ASDs) for systems having unidirectional power flow. The EI-based ASD is mostly attractive due to its improved harmonic performance compared to a conventional ASD. In this paper, the input currents of the EI-based ASD are investigated and compared with the conventional ASDs with respect to interharmonics, which is an emerging power quality topic. First, the DC-link oscillations generation process is analyzed at the inverter level under balanced and unbalanced load conditions, where they are considered as main causes of the interharmonic distortions in the ASD applications. Thereafter, the key role of the EI at the DC stage is investigated in terms of high impedance and current harmonics transfer, and it is compared with the conventional passive filter performance. It is shown that the EI will reduce low-frequency oscillations coming from the load side, and consequently it will give rise to lower-amplitude interharmonics in the input current of the drive. The obtained experiments and simulations for both EI-based and conventional ASD systems verify the proposed theoretical analysis in determining the line input current interharmonics.**

Index Terms—Adjustable speed drives, electronic inductor, harmonics, interharmonics, voltage source converter.

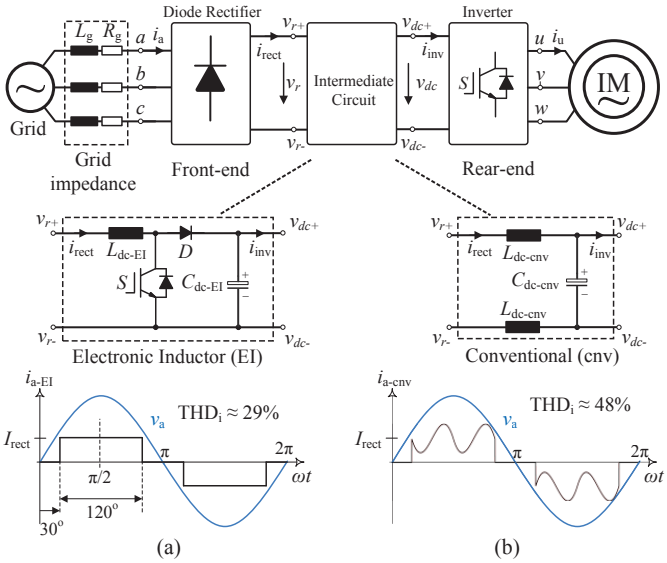

Fig. 1. Typical block representation of an ASD and the input current, (a) With an electrical inductor (EI). (b) With a conventional filter.

I. Introduction

The ASDs contribution to the industrial electricity consumption is rapidly growing as they operate at different demanded frequencies with a flexible control ability, where a high efficiency can also be achieved. However, the harmonic and interharmonic distortions generated by them may simultaneously deteriorate the grid power quality [1]–[5]. As a result, there are especial concerns about the conventional drives functionality, which call for more advanced harmonic and interharmonic reduction strategies in order to insure a high power quality. Meanwhile, EI-based ASDs, where a typical system representation is shown in Fig. 1(a) and compared with a conventional drive (Fig. 1(b)), have demonstrated a promising performance in reducing the drive input current harmonic distortion [6]–[9]. The EI technique is a simple and cost-effective method, and in order to justify the better performance of EI-based ASD systems, its performance from an interharmonic perspective needs to be fully analyzed.

According to IEC 61000-4-7 standard [10], the interharmonic frequency is defined as any frequency below 2 kHz, which is not an integer multiple of the fundamental frequency. The continuous growth of the power electronic applications and more utilization of the ASDs have increased the interharmonic distortion level in the grid. Following that, several grid malfunctions have been reported, where they were caused by the presence of the interharmonics in the power system [11]–[13]. In this respect, the new generation of the modern ASDs such as EI-based ASDs may play an important role in the future in order to improve the grid power quality.

In a typical ASD system, the motor load is usually employed to work at various frequencies, which they are not synchronized with the grid line fundamental frequency. Meanwhile, the interactions between the output side distortions, leaked

to the grid, and the grid side harmonics may give rise to the interharmonic emissions in the line currents. In addition to those interharmonics generated during the ASD's normal operating condition, several other factors, such as the load current imbalance and the motor shaft eccentricity, may lead to the presence of significant interharmonic emissions in the input current of the motor drive. Therefore, the variety of the interharmonic sources is considered as a challenging subject in the conventional ASDs, and there are continuous efforts in research to improve the ASD performance from an interharmonic perspective [14]–[16].

The main aim of this paper is to investigate the input current interharmonic level of the EI-based ASD, with specific emphasis on the balanced and unbalanced load conditions. Moreover, the obtained results are compared with those from the conventional drive at the same operating conditions. It is shown that employing the EI-based ASDs can significantly reduce the input current interharmonic amplitudes compared to the conventional drives. First, in Section II a theoretical analysis introduces the transfer of the harmonics at the inverter level. Thereafter in Section III, the effects of the electronic inductor, and of the conventional passive filters on the harmonic transfer at the DC-link stage are discussed, where they can affect the drive input current interharmonics. Simulation and experimental results are presented in Section IV to verify the effectiveness of the theoretical analysis. Finally, Section V draws the conclusions.

II. Harmonic Transfer at Inverter Level

Fig. 1 shows the schematics of the voltage source inverter fed ASD, where the embedded intermediate circuit can be replaced by an electronic inductor (EI) and/or by a conventional passive filter. Taking the inverter operation into account, the DC-link inverter side voltage v_{dc} is switched on and off by applying an appropriate modulation strategy and it forms the pulsating inverter pole voltages v_x ($x = u,\ v,\ w$) with the desired amplitude and frequency. It is well-accepted in the literature that the inverter switched output voltages are basically periodic with respect to the modulation and modulating signals and they can be interpreted as a waveform composed of a DC quantity V_{dc}, the baseband harmonics, and the carrier group harmonics by applying a double Fourier series solution. Equation (1) represents the general form of this solution [17],

$$\begin{aligned} v_x(t) = \tfrac{A_{00}}{2} + \sum_{n=1}^{\infty} [A_{0n}\cos(n[\omega_o t - p\tfrac{2\pi}{3}]) \\ + B_{0n}\sin(n[\omega_o t - p\tfrac{2\pi}{3}])] \\ + \sum_{m=1}^{\infty}\sum_{n=-\infty}^{\infty} [A_{mn}\cos(m\omega_c t + n[\omega_o t - p\tfrac{2\pi}{3}]) \\ + B_{mn}\sin(m\omega_c t + n[\omega_o t - p\tfrac{2\pi}{3}])] \end{aligned} \tag{1}$$

where ω_o and ω_c denote the fundamental and the carrier angular frequencies.

The harmonic coefficients A_{mn} and B_{mn} should be calculated according to the implemented modulation strategy. In this paper, a symmetrical regularly sampled Space Vector Modulation (SVM) method has been selected as the inverter modulation scheme. The parameter p gets 0, 1 and -1 values for the output phases u, v and w respectively. The output voltages with harmonics, where it feeds an Induction Machine (IM) as a load, will then give rise to the three-phase output currents i_x ($x = u,\ v,\ w$), whose frequency-domain representation can be given as,

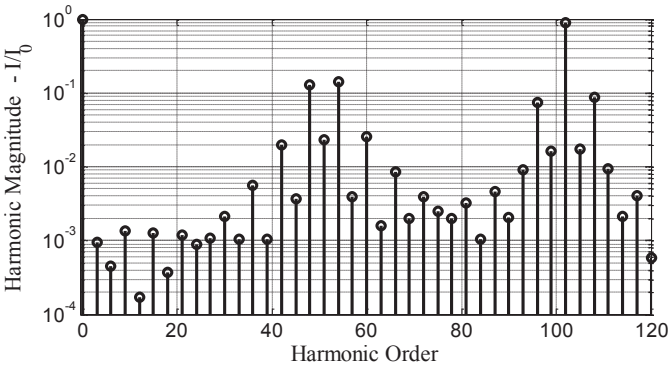

Fig. 2. Theoretical harmonic spectrum of the DC-link inverter side current with the modulation index $M = 0.8$ and pulse ratio $\omega_c/\omega_o = 51$, by applying the symmetrical regularly sampled SVM modulation strategy.

$$\begin{bmatrix} I_u(\omega) \\ I_v(\omega) \\ I_w(\omega) \end{bmatrix} = \frac{V_{dc}}{3Z(\omega)} \begin{bmatrix} 2 & -1 & -1 \\ -1 & 2 & -1 \\ -1 & -1 & 2 \end{bmatrix} \begin{bmatrix} S_u(\omega) \\ S_v(\omega) \\ S_w(\omega) \end{bmatrix} \tag{2}$$

with $Z(\omega)$ being the motor frequency-domain phase impedance. The inverter switching functions S_x ($x = u,\ v,\ w$) can be obtained as,

$$S_x(\omega) = \frac{V_x(\omega)}{V_{dc}}\ , \qquad x \in \{u,\ v,\ w\} \tag{3}$$

The inverter phase switching functions in (3), when multiplied by the associated phase currents, will give rise to DC-link inverter side current i_{inv} containing low and high-frequency oscillations,

$$I_{inv}(\omega) = \sum_{x \in \{u,\ v,\ w\}} S_x(\omega) \otimes I_x(\omega) \tag{4}$$

Fig. 2 illustrates the frequency spectrum of the DC-link inverter side current corresponding to a modulation index $M = 0.8$ with a pulse ratio ω_c/ω_o = 51, when the symmetrical regularly sampled SVM modulation scheme is implemented.

In the case of having a load current imbalance, other exclusive current oscillations may also appear at the immediate DC terminal of the inverter. In this condition, by neglecting the high-frequency components effect, the unbalanced load currents i_x ($x = u,\ v,\ w$) can be expressed as in (5), where they are composed of the positive-sequence i_x^p ($x = u,\ v\ ,\ w$) and the negative-sequence i_x^n ($x = u,\ v,\ w$) components,

$$\begin{aligned} i_x &= i_x^p + i_x^n \\ &= I_o^p\ \sin(\omega_o t + \theta_o^p - p\tfrac{2\pi}{3}) + I_o^n\ \sin(\omega_o t + \theta_o^n + p\tfrac{2\pi}{3}) \end{aligned} \tag{5}$$

TABLE I
Simulation and Experimental Parameters Values.

Symbol	Parameter	Value
$v_{a,b,c}$	Grid phase voltage	230 V_{rms}
f_g	Grid frequency	50 Hz
L_{dc-cnv}	Conventional DC-link inductor	1.25 mH
L_{dc-EI}	EI's inductor	2 mH
C_{dc-cnv}	Conventional DC-Link capacitor	500 μF
C_{dc-EI}	EI's capacitor	470 μF
v_{dc-EI}	EI's DC-link voltage	700 V
k_p, k_i	EI's voltage controller parameters	1.5, 0.05
HB	EI's controller hysteresis band	0.88
v_{LL}	Induction motor rated voltage	380 V_{rms}
P_{IM}	Induction motor rated power	7.5 kW

with $\{I_o^p, I_o^n\}$ and $\{\theta_o^p, \theta_o^n\}$ being the amplitudes and the phase angles of the corresponding positive- and negative-sequence components.

For the sake of simplicity in the unbalanced case, the inverter switching function given in (3) can be represented in the time domain as (6) in which the high-frequency components are not considered,

$$\begin{pmatrix} s_u(t) = S_o \sin(\omega_o t) \\ s_v(t) = S_o \sin(\omega_o t - \frac{2\pi}{3}) \\ s_w(t) = S_o \sin(\omega_o t + \frac{2\pi}{3}) \end{pmatrix} \tag{6}$$

The output unbalanced currents in (5) will then make their contribution to the DC-link inverter side current according to (4) and its time-domain expression is presented in (7),

$$\begin{aligned} i_{inv}(t) &= s_u(t) \cdot i_u(t) + s_v(t) \cdot i_v(t) + s_w(t) \cdot i_w(t) \\ &= \tfrac{3}{2} S_o I_o^p \cos(\theta_o^p) - \tfrac{3}{2} S_o I_o^n \cos(2\omega_o t + \theta_o^n) \end{aligned} \tag{7}$$

According to (7), the unbalanced motor currents may generate oscillations in the DC link at twice the output frequency f_o. These distortions are basically caused by the negative-sequence output currents.

III. Harmonic Transfer at DC-Link and Diode Rectifier Level

The intermediate circuit placed at the DC link is a key player on the harmonic transfer from the inverter side to the rectifier side. The main idea behind employing the electronic inductor is to realize a large inductor behavior, by applying an appropriate control strategy on a DC–DC converter (i.e., boost converter), as it is shown in Fig. 1(a). Thereby, the conventional drives hump-shape input current in the time domain will be replaced by a square-shape waveform and it improves the total current harmonic distortions injected to the grid. However, the low-frequency interharmonic injection into the grid highly depends on the resonance characteristic of the employed intermediate circuit, when it deals with the oscillations coming from the inverter side.

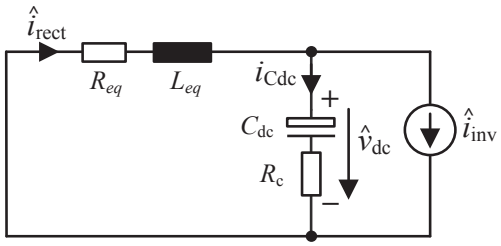

Fig. 3. DC-link equivalent circuit of the conventional drive for output disturbance transfer analysis.

Fig. 3 shows the DC-link equivalent circuit of the conventional ASD to analyze the harmonic transfer from the inverter to the rectifier side. The equivalent DC-link inductance L_{eq} and resistance R_{eq} are defined as,

$$L_{eq} = 2L_{dc-cnv} + 2L_g \tag{8}$$

$$R_{eq} = 2R_{dc-cnv} + 2R_g \tag{9}$$

where the grid inductance and resistance are notated as L_g and R_g, respectively. The DC-link inductance and resistance are also specified by $2L_{dc-cnv}$ and $2R_{dc-cnv}$.

A suitable indicator through which the possible amplification at the DC link can be evaluated, is called the Resonant Factor (RF), and it is defined as [18],

$$RF = \left| \frac{\hat{i}_{rect}}{\hat{i}_{inv}} \right| = \left| \frac{Z_C}{Z_C + Z_L} \right| \tag{10}$$

with $Z_L = R_{eq} + j\omega L_{eq}$ and $Z_C = R_c + 1/(j\omega C_{dc})$.

The resonance characteristics in the EI-based drive should be investigated by using the EI equivalent circuit and its small signal model as presented in Fig. 4. In this respect, the resonance factor defined in (10) for the conventional drive can be utilized by obtaining the closed-loop response in the EI-based drive, and it can be given as,

$$RF = \left| \frac{\hat{i}_L(j\omega)}{\hat{i}_{Load}(j\omega)} \Big|_{\hat{v}_i(j\omega), \hat{v}_{ref}=0} \right| \tag{11}$$

where $\hat{i}_L(j\omega) = \hat{i}_{rect}(j\omega)$. According to this condition and based on Fig. 4(c) the following relationships can be obtained,

$$\begin{aligned} \hat{d} &= F_m \left[-R_f H_1 G_c \hat{v}_{dc} - R_f H_2 \hat{i}_L - F_v \hat{v}_{dc} \right] \\ \hat{i}_L &= G_{id}\hat{d} + \frac{Z_{out}}{j\omega L_e} \quad \hat{i}_{Load} \\ \hat{v}_{dc} &= G_{vd}\hat{d} - Z_{out}\hat{i}_{Load} \end{aligned} \tag{12}$$

$$RF = \left| \frac{\hat{i}_L(j\omega)}{\hat{i}_{Load}(j\omega)} \Big|_{\hat{v}_i(j\omega), \hat{v}_{ref}=0} \right| = Z_{out}(j\omega) \times \frac{1 + F_m(R_f H_1 G_c G_{vd} + F_v G_{vd}) + j\omega L_e G_{id} F_m (R_f H_1 G_c + F_v)}{j\omega L_e (1 + F_m (R_f H_1 G_c G_{vd} + F_v G_{vd} + R_f H_2 G_{id}))} \tag{13}$$

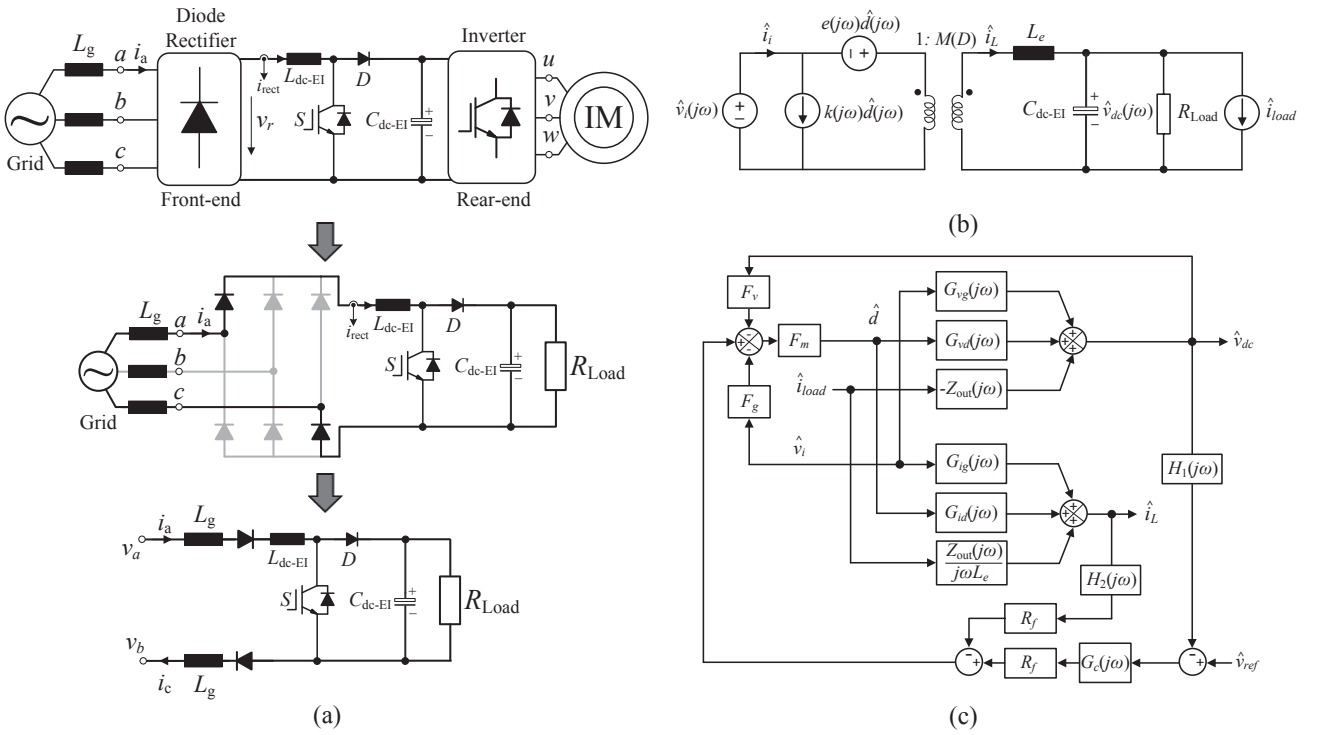

Fig. 4. (a) Equivalent circuit of the EI-based drive for system analysis, (b) Small signal model of the EI-intermediate drive, (c) Mathematical model of the converter (EI) operating in current mode control.

Thus, by using (11) and (12), the RF for the EI-based drive can be given as (13), where Z_{out} represents the open-loop output impedance of the converter as,

$$Z_{out}\left(j\omega\right)=\frac{\hat{v}_o\left(j\omega\right)}{-\hat{i}_{load}\left(j\omega\right)}\Big|_{\hat{d}(j\omega),\hat{v}_i(j\omega)=0}=\frac{j\omega L_e}{1-\omega^2 L_e C_{dc-EI}+\dfrac{j\omega L_e}{R_{Load}}} \tag{14}$$

Here H_1, H_2 and R_f are the voltage and current sensing transfer functions and gains, which depend on the used sensors. Moreover, G_{vd} and G_{id} are small-signal open-loop transfer functions, which are defined as [19]–[21],

$$G_{vd}\left(j\omega\right)=\frac{\hat{v}_{dc}\left(j\omega\right)}{\hat{d}\left(j\omega\right)}\Big|_{\hat{v}_i(j\omega),\hat{i}_{Load}(j\omega)=0}=\frac{M\left(D\right)k\left(j\omega\right)}{1-\omega^2 L_e C_{dc-EI}+\dfrac{j\omega L_e}{R_{Load}}} \tag{15}$$

$$G_{id}\left(j\omega\right)=\frac{\hat{i}_L\left(j\omega\right)}{\hat{d}\left(j\omega\right)}\Big|_{\hat{v}_i(j\omega),\hat{i}_{Load}(j\omega)=0}=\frac{M\left(D\right)k\left(j\omega\right)\left(\frac{1}{R_{Load}}+j\omega C_{dc-EI}\right)}{1-\omega^2 L_e C_{dc-EI}+\dfrac{j\omega L_e}{R_{Load}}} \tag{16}$$

Notably, $G_c(j\omega)$ is the voltage controller transfer function, which here is implemented based on a Proportional-Integral (PI) controller,

$$G_c\left(j\omega\right)=k_p+\frac{k_i}{j\omega} \tag{17}$$

In addition, the current controller gains are given in Table II. These parameters are calculated for the hysteresis current control operation [19], [20].

Fig. 5 shows the resonance factor RF plotted by using equations (10) and (13), where the conventional passive filter components and the EI have been employed as the DC-link intermediate circuit. The associated circuit parameters for drawing the plot are listed in Table I. As it can be seen, the

TABLE II
BOOST CONVERTER CANONICAL MODEL PARAMETERS WITH CURRENT CONTROLLED GAINS.

$M(D)$	L_e	$e(j\omega)$	$k(j\omega)$	F_m	F_g	F_v
$\frac{V_{dc}}{V_i}=\frac{1}{(1-D)}$	$\frac{L_{dc-EI}+2L_g}{(1-D)^2}$	$V_{dc}\left(1-\frac{j\omega L_{dc-EI}}{(1-D)^2R_{Load}}\right)$	$\frac{V_{dc}}{(1-D)^2R_{Load}}$	$\frac{-2(L_{dc-EI}+2L_g)}{T_sV_{dc}}$	$\frac{(1-D)T_s}{2(L_{dc-EI}+2L_g)}$	$-\frac{T_s}{2(L_{dc-EI}+2L_g)}$

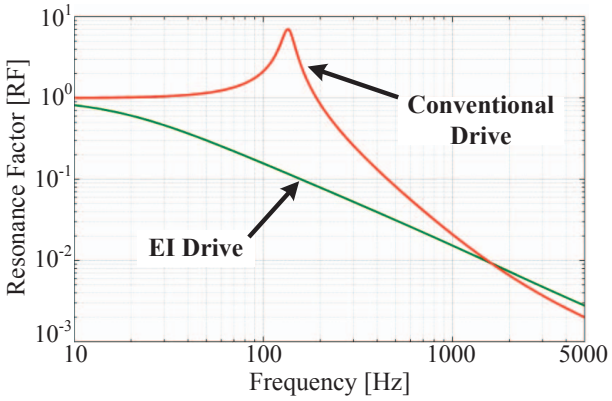

Fig. 5. DC-link Resonance Factor RF in the conventional and EI-based drive.

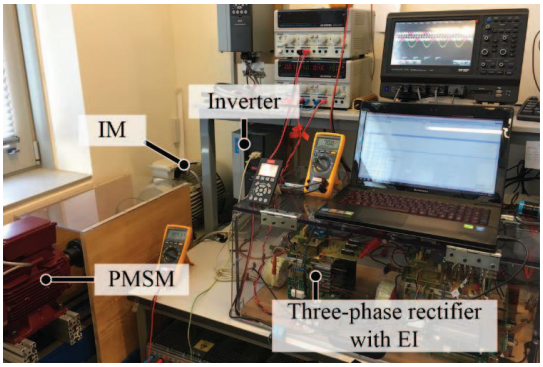

Fig. 6. Laboratory setup of the conventional and EI-based drives, and an Induction Motor IM coupled with a Permanent Magnet Synchronous Machine PMSM as a load.

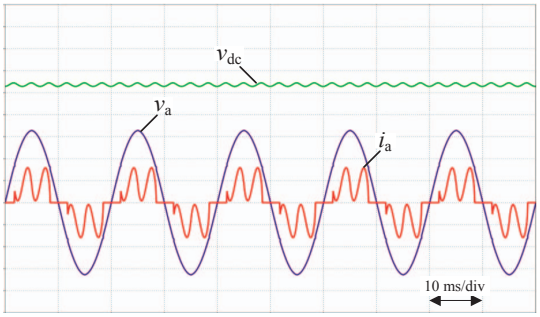

Fig. 7. Simulated line voltage v_a (100 V/div), input current i_a (10 A/div), and DC-link voltage v_{dc} (100 V/div) waveforms, when the conventional drive operates at the output frequency f_o =40 Hz and the load torque T_L =34 Nm.

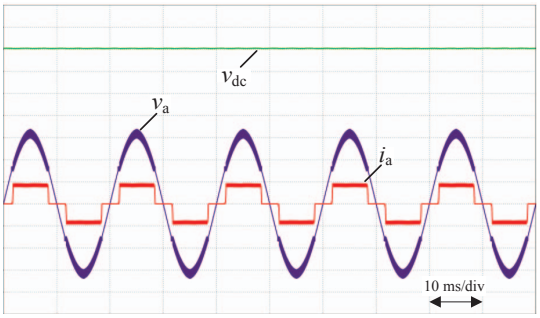

Fig. 8. Simulated line voltage v_a (100 V/div), input current i_a (10 A/div), and DC-link voltage v_{dc} (100 V/div) waveforms, when the EI-based drive operates at the output frequency f_o =40 Hz and the load torque T_L =34 Nm.

inverter side low-frequency oscillations, when passing through the DC stage, will be attenuated in the case of applying the EI-based intermediate circuit, whereas the presence of the resonance peak caused by employing the conventional passive filter components can intensify those oscillations. Consequently, under the same operating conditions, the DC-link inverter side oscillations would appear with lower amplitude at the immediate DC terminal of the diode rectifier by implementing the EI instead of using the conventional passive filter.

Finally, the DC-link rectifier side oscillations, which have already been caused by the inverter operation and have passed through the DC stage, will be modulated by the front-end diode rectifier switching function $S_{ph}(t)$ as,

$$i_{ph}(t) = S_{ph}(t)\, i_{rect}(t) \tag{18}$$

$$S_{ph}(t) = \frac{2\sqrt{3}}{\pi}\left(\cos(\omega_g t + \theta_{ph}) \pm \sum_{k=1}^{\infty} \frac{\cos\left[(6k \pm 1)(\omega_g t + \theta_{ph})\right]}{6k \pm 1}\right) \tag{19}$$

where $ph = a$, b, or c and $\omega_g = 2\pi f_g$ with θ_a, θ_b, and θ_c equal to 0, -120 and 120, respectively. Following (18) and (19), the DC-link harmonics f_{h-dc}, generated according to (4) and (7), will appear as the line current interharmonics with the frequencies f_{ih} as,

$$f_{ih} = \left|\left[6(\Lambda - 1) \pm 1\right] f_g \pm f_{h-dc}\right|, \qquad \Lambda = 1, 2, 3, .. \tag{20}$$

In this respect, further suppression of the output side distortions at the DC-link stage, which can be achieved by using the EI, may result in lower amplitude interharmonics in the drive input current.

IV. Simulation and Experimental Results

In order to validate the theoretical analysis, a series of PLECS simulations and experiments have been performed on 7.5 kW conventional and EI-based ASD, according to the configurations shown in Fig. 1. The ASD specifications have been listed in Table I. Fig. 6 shows a picture of the employed laboratory experimental setups. Notably, the Induction Motor IM is controlled by a constant Voltage-to-Frequency V/F approach and the Space Vector Modulation SVM scheme has been applied on the inverter. In the experimental tests, a 6 kW Permanent Magnet Synchronous Machine PMSM is also coupled with the IM to work as a load. Moreover, a Chroma three-phase grid simulator has been employed in order to reduce the grid background distortions.

Figs. 7 and 8 illustrate the simulated line voltage, input current and DC-link voltage waveforms of the conventional and the EI-based drives, when the motor operates at the output frequency $f_o = 40$ Hz and the load torque $T_L = 34$ Nm. It is worth to note that in the EI-based drive, the DC-link inductor current i_{rect} is controlled to be kept constant irrespective of

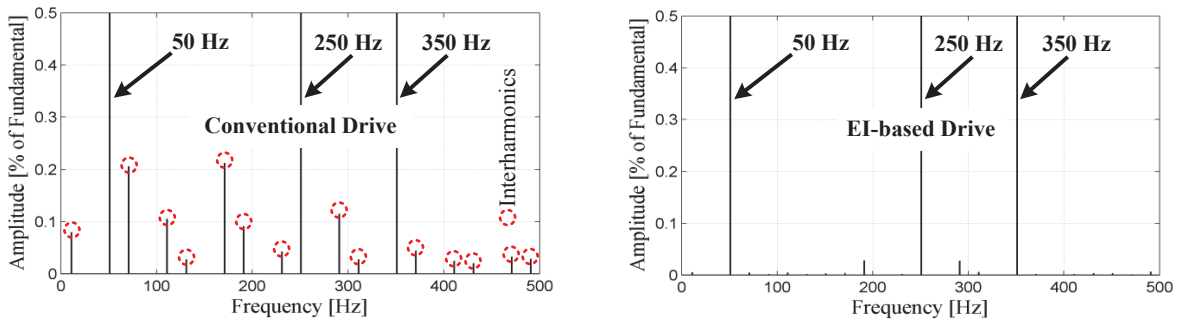

(a) (b)

Fig. 9. Simulated drive input current (i.e., i_a in Fig. 1) spectrum at an output frequency $f_o = 40$ Hz, the switching frequency $f_{sw} = 3$ kHz and the load torque $T_L = 34$ Nm: (a) Conventional drive, (b) EI-based drive.

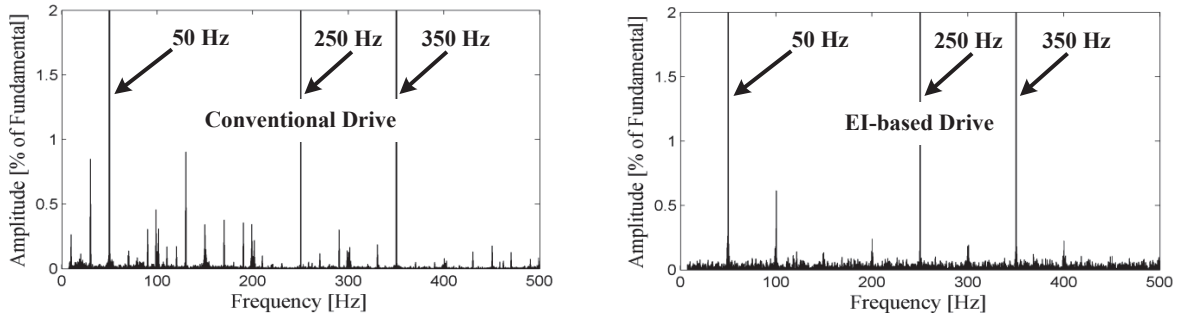

(a) (b)

Fig. 10. Measured drive input current (i.e., i_a in Fig. 1) spectrum at an output frequency $f_o = 40$ Hz, the switching frequency $f_{sw} = 5$ kHz and the load torque $T_L = 34$ Nm: (a) Conventional drive, (b) EI-based drive.

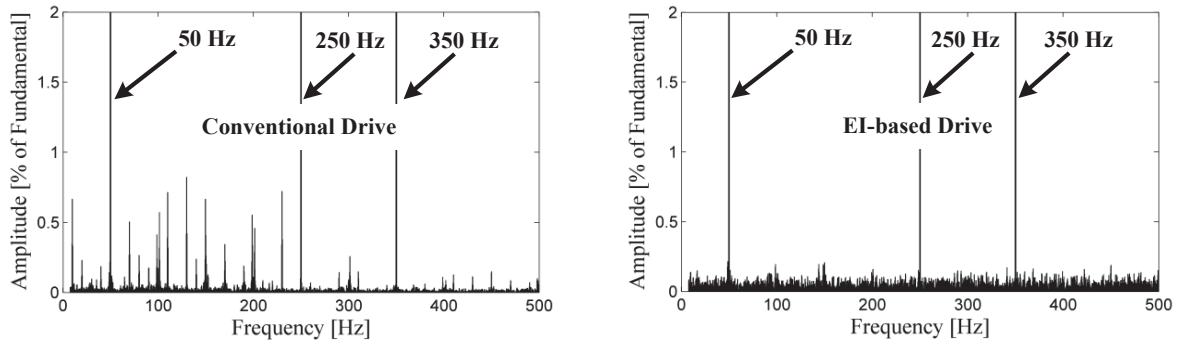

(a) (b)

Fig. 11. Measured drive input current (i.e., i_a in Fig. 1) spectrum at an output frequency $f_o = 30$ Hz, the switching frequency $f_{sw} = 5$ kHz and the load torque $T_L = 28$ Nm: (a) Conventional drive, (b) EI-based drive.

the output power level. As a result, the input current i_a of the EI-based drive will be a square-shape waveform (see Fig. 8), and it will give rise to lower input current Total Harmonic Distortion THD compared to the conventional drive.

The input current i_a frequency spectra of the conventional and EI-based drives have been shown in Fig. 9, where the rear-end inverter feeds the motor load at the output frequency $f_o = 40$ Hz, the load torque $T_L = 34$ Nm, and the switching frequency $f_{sw} = 3$ kHz. As it can be observed, the conventional drive injects low-frequency interharmonics into the grid (see Fig. 9(a)), whereas these distortions have been significantly attenuated by employing the EI-based drive (see Fig. 9(b)). This characteristic can also be found by referring to Fig. 5, where employing the EI will impose more low-frequency attenuation at the DC-link compared to the conventional passive filter, and consequently, it will give rise to lower-amplitude input current interharmonic components at the same operating conditions.

The investigation has then been followed experimentally at the inverter switching frequency $f_{sw} = 5$ kHz. Fig. 10 illustrates the input current frequency spectra at the output frequency $f_o = 40$ Hz and the load torque $T_L = 34$ Nm. It

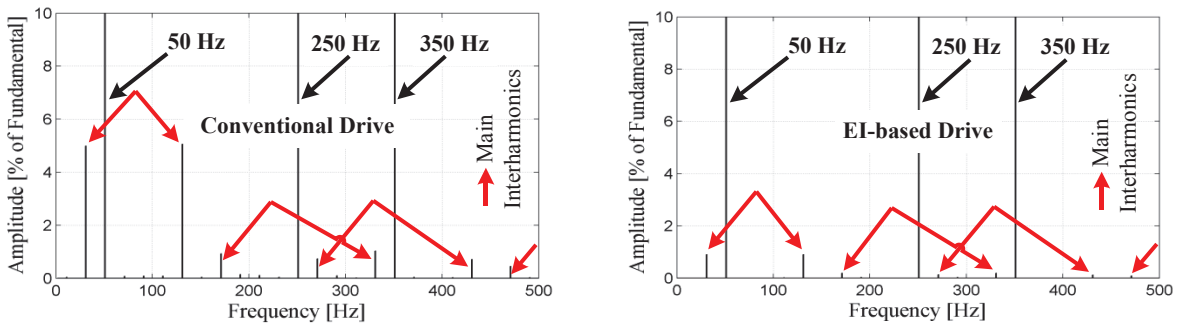

Fig. 12. Simulated drive input current (i.e., i_a in Fig. 1) spectrum with five percent load current imbalance at the output frequency $f_o = 40$ Hz and the load torque $T_L = 40$ Nm: (a) Conventional drive, (b) EI-based drive.

is evident that the interharmonic distortions existing in the input current of the conventional drive (as it is shown in Fig. 10(a)) have been reduced by employing the EI-based drive (Fig. 10(b)). Further experimental examinations of the drives input current interharmonic performance have been performed at the output frequency $f_o = 30$ Hz and the load torque $T_L = 28$ Nm. The obtained results have been presented in Fig. 11. As it can be seen, the EI-based drive shows superior performance with respect to the input current low-frequency interharmonic emissions.

Finally, the drives input current interharmonic evaluation was followed by introducing about five percent motor current imbalance. As it is mentioned in Section II, the unbalanced motor currents can give rise to a second order (of the output frequency f_o) oscillation at the DC link. These distortions, when interacting with the input current harmonics of the ASD, can produce interharmonics in the grid side. Fig. 12(a) shows the conventional drive input current frequency spectrum at the output frequency $f_o = 40$ Hz and the load torque $T_L = 40$ Nm. It is evident that the high-amplitude interharmonic components have been injected into the grid, where they are actually distributed around the grid fundamental frequency component and also around the major harmonics. The EI-based drive interharmonic performance with the presence of five percent output current imbalance has been illustrated in Fig. 12(b). The obtained results indicate that the EI-based drive decreases significantly the input current interharmonics, as a result of remarkable low-frequency suppression that it would impose on the oscillations at the DC-link stage.

V. Conclusion

In this paper, the EI-based ASD input currents are evaluated in terms of low-frequency interharmonic distortions, and its performance has been compared with the conventional drives. It has been shown that the drive input current interharmonic amplitudes will be significantly reduced, if the DC-link passive filter is replaced with an Electronic Inductor EI. This characteristic has been demonstrated by analyzing the resonance behaviour of the DC-link intermediate circuits in the employed drives. In this respect, the EI intermediate circuit would suppress the output side oscillations, when they pass through the DC stage, and it will eventually give rise to lower-amplitude interharmonics compared to using the passive filter elements. The interharmonic distortion improvement has particularly been highlighted in the presence of the load current imbalance by applying the EI, whereas the high-amplitude interharmonics can be injected into the grid at the same operating conditions by employing a passive filter. The presented simulation and experimental results have validated the proposed theoretical analysis.

References

[1] J. W. Gray and F. J. Haydock, "Industrial power quality considerations when installing adjustable speed drive systems," *IEEE Trans. Ind. Appl.*, vol. 32, no. 3, pp. 646–652, May/Jun.1996.

[2] F. Zare, "Harmonics issues of three-phase diode rectifiers with a small DC link capacitor," in *Proc. IEEE-PEMC Conf.*, 2014, pp. 912–917.

[3] M. Rifai, T. H. Ortmeyer, and W. J. McQuillan, "Evaluation of current interharmonics from AC drives," *IEEE Trans. Power Del.*, vol. 15, no. 3, pp. 1094–1098, Jul. 2000.

[4] F. De Rosa, R. Langella, A. Sollazzo, and A. Testa, "On the interharmonic components generated by adjustable speed drives," *IEEE Trans. Power Del.*, vol. 20, no. 4, pp. 2535–2543, Oct. 2005.

[5] D. Basic, "Input current interharmonics of variable-speed drives due to motor current imbalance," *IEEE Trans. Power Del.*, vol. 25, no. 4, pp. 2797–2806, Oct. 2010.

[6] J. W. Kolar and T. Friedli, "The essence of three-phase PFC rectifier systems—Part I," *IEEE Trans. Power Electron.*, vol. 28, no. 1, pp. 176–198, Jan. 2013.

[7] C. Klumpner, F. Blaabjerg, and P. Thogersen, "Converter topologies with low passive components usage for the next generation of integrated motor drives," in *Proc. IEEE-PESC Conf.*, 2003, pp. 568–573.

[8] P. Davari, Y. Yang, F. Zare, and F. Blaabjerg, "A multi-pulse pattern modulation scheme for harmonic mitigation in three-phase multi-motor drives," *IEEE J. Emerg. Sel. Top. Power Electron.*, vol. 4, no. 1, pp. 174–185, Mar. 2016.

[9] P. Davari, F. Zare, and F. Blaabjerg, "Pulse Pattern-Modulated Strategy for Harmonic Current Components Reduction in Three-Phase AC–DC Converters," *IEEE Trans. Ind. Appl.*, vol. 52, no. 4, pp. 3182–3192, Jul./Aug. 2016.

[10] *Electromagnetic compatibility (EMC)—Part 4-7: Testing and Measurement TechniquesGeneral Guide on Harmonics and Interharmonics Measurements and Instrumentation, for Power Supply Systems and Equipment Connected Thereto*, IEC Std. 61000-4-7., 2009.

[11] F. Wang and M. Bollen, "Measurement of 182 Hz interharmonics and their impact on relay operation," in *Proc. IEEE-ICHQP Conf.*, 2000, pp. 55–60.

[12] S. K. Ronnberg, M. H. Bollen, and M. Wahlberg, "Interaction between narrowband power-line communication and end-user equipment," *IEEE Trans. Power Del.*, vol. 26, no. 3, pp. 2034–2039, Jul. 2011.

[13] J. Yong, X. Li, and W. Xu, "Interharmonic Source Model for Current Source Inverter Fed Variable Frequency Drive," *IEEE Trans. Power Del.*, vol. PP, no. 99, pp. 1–1, Apr. 2016.
[14] H. Soltani, P. C. Loh, F. Blaabjerg, and F. Zare, "Sources and mitigation of interharmonics in back-to-back controllable drives," in *Proc. IEEE-EPE*, 2014, pp. 1–9.
[15] W. Cho, E. J. Powers, and S. Santoso, "Mitigation of harmonic and interharmonic effects using a dithering method in adjustable speed drives," in *Proc. Instrum. Meas. Technol. Conf.*, 2010, pp. 1481–1485.
[16] H. Soltani, P. Davari, P. C. Loh, F. Blaabjerg, and F. Zare, "Input current interharmonics in adjustable speed drives caused by fixed-frequency modulation techniques," in *Proc. IEEE-APEC*, 2016, pp. 229–235.
[17] D. G. Holmes and T. A. Lipo, *Pulse width modulation for power converters: principles and practice*. New York: IEEE Press, 2003.
[18] H. Soltani, F. Blaabjerg, F. Zare, and P. C. Loh, "Effects of passive components on the input current interharmonics of adjustable-speed drives," *IEEE J. Emerg. Sel. Top. Power Electron.*, vol. 4, no. 1, pp. 152–161, Mar. 2016.
[19] R. Ahmadi and M. Ferdowsi, "Modeling closed-loop input and output impedances of DC-DC power converters operating inside dc distribution systems," in *Proc. IEEE-APEC Conf.*, 2014, pp. 1131–1138.
[20] J. H. Park and B. H. Ch, "Small signal modeling of hysteretic current mode control using the PWM switch model," in *IEEE Workshops on Computers in Power Electronics*, 2006, pp. 225–230.
[21] R. W. Erickson and D. Maksimovic, *Fundamentals of power electronics*. Springer Science & Business Media, 2007.